Contents lists available at ScienceDirect

Simulations of thixotropic liquids

J.J. Derksen

Chemical & Materials Engineering, University of Alberta, Edmonton, AB, Canada T6G 2G6

ABSTRACT

In thixotropic liquids the rheological properties depend on the liquid's deformation history. Clay suspensions (as encountered in oil sands mining) are a prominent example. Activated clay particles form a network. As a consequence of (ionic) transport limitations, the network is not an instantaneous feature; it takes time to build up, and also to break down, the latter as a result of deformation in the liquid. In this paper a procedure for detailed simulations of flow of viscous thixotropic liquids is outlined. The local viscosity of the liquid relates to the level of integrity of the network. The time-dependence of the liquid's rheology is due to the finite rate with which the network in the liquid builds up or breaks down. This concept has been incorporated in a lattice-Boltzmann discretization of the flow equations. With this methodology the way thixotropic liquids are mobilized in mixing tanks and the drag force experienced by dense assemblies of coarse particles (e.g. sand) in thixotropic liquids have been studied.

© 2010 Elsevier Inc. All rights reserved.

1. Introduction

Many processing and mixing applications involve complex liquids. Examples are specifically abundant in food, pharmaceutical, and related industries; paper and pulp; polymer processing; and also oil sands mining and operations; the latter being the major motivation of the present work. One of the many intriguing phenomena that can occur in complex liquids is the development of a yield stress. Usually the yield stress is the consequence of a network being generated as a result of particle–particle or (macro-) molecular interactions of agents dispersed in a carrier phase. For example, in oil sands processing [1] clay particles get surface activated by (hot) water injection which initiates long range interactions between them. As a result of (ionic) transport limitations, the network is not an instantaneous feature; it takes time to build up, and also to break down as a result of deformations in the liquid. In non-homogeneous flows such time-dependent rheology (usually termed thixotropy) is closely linked to the flow dynamics as the (also non-homogeneous) level of network integrity is transported with the flow. It is expected that, from a fluid dynamics point of view, interesting situations occur when the time scales related to the network interfere with characteristic flow time scales.

In the applications that motivate the present work, geometrical complexity of the flows is an essential feature. On the macro-scale one could think of flows in agitated vessels, or separation devices such as hydrocyclones. In many cases such process equipment operates in turbulent or (as is often the case with relatively viscous non-Newtonian liquids) transitional flow regimes. Also on the meso-scale geometrical complexity matters: e.g. dense liquid–solid suspensions with complex interstitial liquid domains and moving solid particles. In any case: realistic numerical simulations of such flows require flexibility in setting up computational grids, and above all computational efficiency in order to be able to resolve the flow to a sufficient level of detail. Previous studies [2,3] have shown that the lattice-Boltzmann method [4] is a versatile procedure for performing highly resolved computational fluid dynamics of Newtonian fluids. In this paper lattice-Boltzmann simulations of flows of thixotropic liquids in complexly shaped confinements at meso- and macro-scale are discussed.

E-mail address: jos@ualberta.ca

A troubling issue regarding simulating non-Newtonian rheology is the steep increase of the number of parameters with increasing complexity of the model characterizing the liquid, and the need to (experimentally and/or computationally) determine their values. For this reason we choose to limit the number of parameters by adopting a relatively simple thixotropy model.

2. Thixotropy model

The thixotropy model that has been adopted is based on early work due to Storey and Merrill [5] and Moore [6], more recently reviewed and applied in [7]. In this purely viscous (i.e. non-elastic) model we keep track of a scalar λ that varies between 0 and 1 and indicates the integrity of the network ($\lambda = 0$: no network; $\lambda = 1$: fully developed network). Its transport equation reads

$$\frac{\partial \lambda}{\partial t} + u_i \frac{\partial \lambda}{\partial x_i} = -k_1 \dot{\gamma} \lambda + k_2 (1 - \lambda) \qquad (1)$$

(summation over repeated indices) with u_i the ith component of the fluid velocity vector and $\dot{\gamma} = \sqrt{2 d_{ij} d_{ij}}$ a generalized deformation rate; $d_{ij} = \frac{1}{2} \left(\frac{\partial u_j}{\partial x_i} + \frac{\partial u_i}{\partial x_j} \right)$ is the rate of strain tensor. The first term on the right hand side of Eq. (1) indicates breakdown of the network due to liquid deformation; the second term is responsible for build-up of the network with a time constant k_2^{-1} associated to it. In the model, the apparent viscosity μ_a is linked to the network integrity according to

$$\mu_a = \mu_\infty (1 + \alpha \lambda). \qquad (2)$$

In a homogeneous shear field with shear rate $\dot{\gamma}$, the steady-state viscosity is

$$\mu_{ss} = \mu_\infty \left(1 + \alpha \frac{k_2}{k_1 \dot{\gamma} + k_2} \right) = \mu_\infty \left(1 + \alpha \frac{\dot{\gamma}_c}{\dot{\gamma} + \dot{\gamma}_c} \right). \qquad (3)$$

The parameter μ_∞ can thus be interpreted as the infinite-shear viscosity; the zero-shear viscosity is $\mu_\infty (1 + \alpha)$; and $\dot{\gamma}_c \equiv \frac{k_2}{k_1}$ is the shear rate at which the liquid typically transits from infinite-shear to zero-shear viscosity. A typical representation of the steady-state rheology (Eq. (3)) is given in Fig. 1. The thixotropic liquid as defined by Eqs. (1) and (2) has four parameters μ_∞, α, k_1, and k_2.

3. Flow solver and scalar transport modeling

The lattice-Boltzmann method (LBM) is a well-established way to numerically solve the incompressible Navier–Stokes equations. The method originates from the lattice-gas automaton concept as conceived by Frisch et al. in 1986 [8]. Lattice gases and lattice-Boltzmann fluids can be viewed as fictitious particles moving over a regular lattice, and interacting with one another at lattice sites. These interactions (collisions) give rise to viscous behavior of the fluid, just as colliding/interacting molecules do in real fluids. Since 1987 particle-based methods for mimicking fluid flow have evolved strongly, as can be witnessed from review articles and text books [4,9,10].

The main reasons for employing the LBM for fluid flow simulations are its computational efficiency and its inherent parallelism, both not being hampered by geometrical complexity. More recently LBM has been applied to non-Newtonian fluid mechanics [11,12].
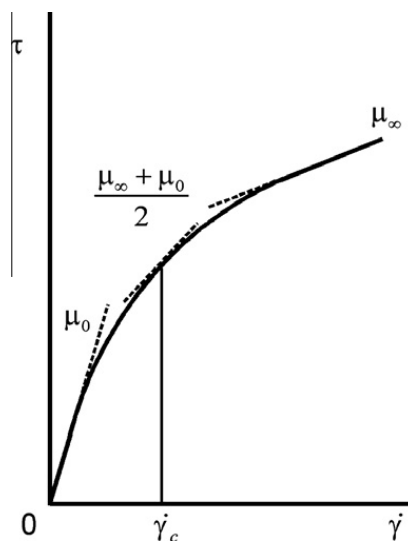

Fig. 1. Steady-state rheology (Eq. (3)) with $\dot{\gamma}_c \equiv \frac{k_2}{k_1}$ and $\mu_0 \equiv \mu_\infty (1 + \alpha)$.

In this paper the LBM formulation of Somers [13] has been employed which falls in the category of three-dimensional, 18 speed (D3Q18) models. Its grid is uniform and cubic. Planar, no-slip walls naturally follow when applying the bounce-back condition. For non-planar and/or moving walls (in case we are simulating the flow in a mixing tank with a revolving impeller) an adaptive force field technique (also known as immersed boundary method) has been used [2,14]. This method has been employed and validated extensively in previous studies involving (turbulent) flow in process equipment [15,16].

For incorporating thixotropy, the viscosity needs to be made dependent on the local value of the network parameter λ (Eq. (2)), and (more importantly) the transport equation for the network parameter (Eq. (1)) needs to be solved. Solving scalar transport equations in a LBM context is an option (see e.g. [17]). It is, however, a relatively expensive approach in terms of computer memory usage: in order to solve for a single scalar we need to allocate as much memory as for solving the Navier–Stokes equations (i.e. 18 real values per lattice node in an 18 speed LBM).

Instead Eq. (1) is solved with an explicit finite volume discretization on the same (uniform and cubic) grid as the LBM; this way only two real values per lattice node need to be stored. An additional advantage of employing a finite volume formulation is the availability of methods for suppressing numerical diffusion. This is particularly important in the present application since Eq. (1) does not have a molecular or turbulent diffusion term; in order to correctly solve Eq. (1) we cannot afford to have significant numerical diffusion. As in previous works [18,19], TVD discretization with the Superbee flux limiter for the convective fluxes [20] was employed. Time-stepping is achieved with an Euler explicit scheme.

4. A benchmark: plane Poiseuille flow

Consider the flow between two fixed parallel plates at mutual distance H driven by a body force (force per unit volume) f_0 in the wall-parallel direction (see Fig. 2 for a definition of the flow and its coordinate system where $z = 0$ corresponds to the centerline of the channel). The body force results in a linear shear stress profile in the liquid: $\tau_{zx} = -f_0 z$. In zero-inertia flow this directly translates in a shear rate $\dot{\gamma} = \left| \frac{-f_0 z}{\mu_a(z,t)} \right|$. Given Eq. (1), and since the system is homogeneous in x-direction the transport equation in the network parameter can be written as

$$\frac{\partial \lambda}{\partial t} = -k_1 \lambda \frac{f_0|z|}{\mu_\infty(1 + \alpha\lambda)} + k_2(1 - \lambda). \tag{4}$$

In the center of the channel ($z = 0$), Eq. (4) implies that λ depends on time according to an exponential function with time constant k_2^{-1}. In order to compare the implications of Eq. (4) for the way the network integrity parameter and the velocity field depend on space (z) and time, it was integrated numerically (with a fourth-order Runge–Kutta scheme) for z in the range $-\frac{H}{2} < z < \frac{H}{2}$. This provides us with a representation of $\lambda(z, t)$ that subsequently is used to determine $\mu_a(z, t)$ (with help of Eq. (2)) and integrate the velocity profile from the notion that $\frac{\partial u_x}{\partial z} = -\frac{f_0 z}{\mu_a}$ with $u_x = 0$ at $z = \pm\frac{H}{2}$. The results of this semi-analytical exercise can be directly compared with our numerical simulations.

In the simulations we start from a zero flow field of Newtonian liquid. Once that flow has fully developed (to a parabolic velocity profile in this case) the thixotropic rheology is switched on and we monitor the development of the network and associated apparent viscosity and velocity field. As the velocity scale the centerline velocity of the Newtonian liquid has been taken: $u_0 = \frac{1}{8} \frac{f_0}{\mu_\infty} H^2$; the Reynolds number has been defined as $\text{Re} = \frac{\rho u_0 H}{\mu_\infty}$. The results in Fig. 3 show very good agreement of the simulations and the semi-analytical solution. The time scales over which the flow switches from the Newtonian steady state to the non-Newtonian steady state, as well as the profiles of λ and u_x are well represented by the simulations. We see the development of the λ-profile in time: starting from zero λ increases quickest in the center of the channel where there is no deformation. Roughly at $t = 50 \frac{H}{u_0} = \frac{2.5}{k_2}$ after switching on the thixotropic rheology the λ profile is close to steady. In the same time range the velocity profile has adapted itself to the new rheology; it has evolved from parabolic to more plug-flow like.

The assumption of zero-inertia as inferred to obtain the semi-analytical solution appears critical. In the right panel of Fig. 3 we compare (at a single moment in time) the semi-analytical solution with simulation results at different Reynolds
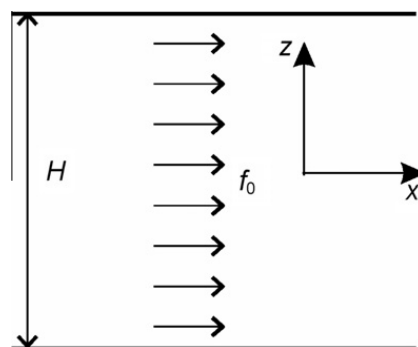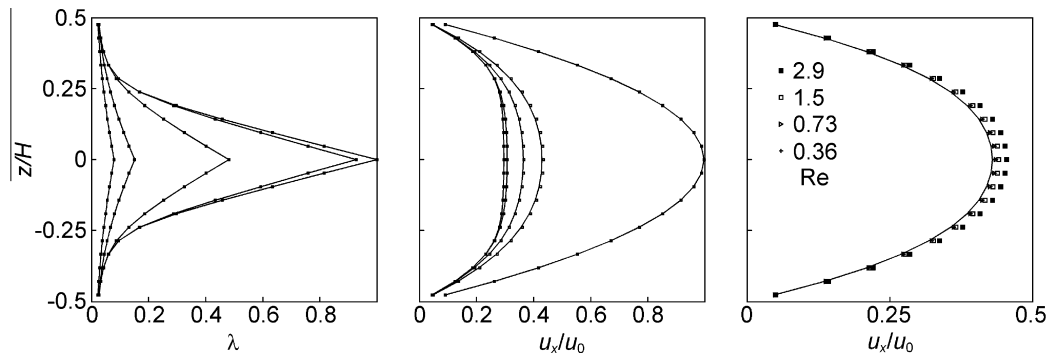

Fig. 2. Plane Poiseuille flow definition.

Fig. 3. Left: λ profiles at various moments (tu_0/H = 1.6, 3.3, 13, 52, and 210; λ *increases* with time) after switching on thixotropic rheology. Middle: velocity profiles (tu_0/H = 0, 1.6, 3.3, 13, and 52; velocity *decreases* with time). Right: velocity profiles at tu_0/H = 1.6 for four different Reynolds numbers. The left and middle panel have Re = 0.73. Drawn curves: semi-analytical solutions; symbols: simulations.

numbers. The trend is that the agreement clearly benefits from reducing the Reynolds number in the simulations. The results with Re < 1 can hardly be distinguished and are close to the semi-analytical solution.

5. Thixotropic liquids in mixing tanks

We now turn to flows of thixotropic liquids in mixing tanks. The geometry of the mixing tank and the impeller are given in Fig. 4, along with a definition of the coordinate system. The impeller, a Rushton turbine, is a de-facto standard impeller in mixing research and therefore allows for comparison with a large body of numerical and experimental data regarding Newtonian and (to a lesser extent) non-Newtonian liquids. It consists of a round disk with six flat blades mounted on its perimeter. The tank has baffles at its perimeter that enhance mixing as they prevent the liquid from rotating largely as a solid body under the influence of the revolving impeller. In this standard configuration all tank and impeller dimensions can be derived from the tank diameter T (see Fig. 4), e.g. the impeller diameter $D = T/3$.

In mixing of Newtonian liquids in stirred tanks the Reynolds number is traditionally defined as $Re = \frac{\rho ND^2}{\mu}$ with N the impeller speed (in rev/s). In analogy the Reynolds number has been defined as $Re = \frac{\rho ND^2}{\mu_\infty}$. The additional three dimensionless numbers if thixotropic liquid mixing is being considered are chosen as follows: $Db = \frac{N}{k_2}$ the Deborah number (the ratio of liquid over flow time scale), $S = \frac{k_2}{k_1} \frac{1}{N} \equiv \frac{\dot{\gamma}_c}{N}$ the dimensionless shear rate number, and α where $\alpha + 1$ is a viscosity ratio.

The tanks to be simulated are of lab-scale size with a tank volume of typically 10 l. A 10 l tank with geometrical layout as given in Fig. 4 has a diameter T = 0.234 m. The impeller diameter $D = T/3$ = 0.078 m. With a liquid having $\mu_\infty = 10^{-2}$ Pa s and $\rho = 10^3$ kg/m^3 mildly turbulent flow is generated if the impeller spins with N = 10 rev/s: Re = $6 \cdot 10^3$. Commonly used thixotropic liquids have time constants in the range of 0.1–10 s (see e.g. [21]), so that the Deborah numbers fall in the range 1–100. To end up with laminar flow if the network would be fully developed (λ = 1 everywhere) we set $\alpha + 1$ = 100. To limit the parameter space, we set the shear rate number to the fixed value of S = 1 which represents the situation with the typical shear rate in the tank (that scales with N) being the same as the liquid's characteristic shear rate $\dot{\gamma}_c$.

As mentioned above, the liquid flow dynamics were resolved using the lattice-Boltzmann method. In its basic implementation (as used in this study) the method applies a uniform, cubic grid. The spatial resolution of the grid was such that the tank diameter T equals 180 grid spacings Δ. The time step is such that the impeller revolves once in 2000 time steps. The rotation of the impeller in the static grid is represented by an immersed boundary technique. As the default situation, the simulations were started from a zero liquid velocity field and a uniform network parameter λ = 0 (no network). Our primary
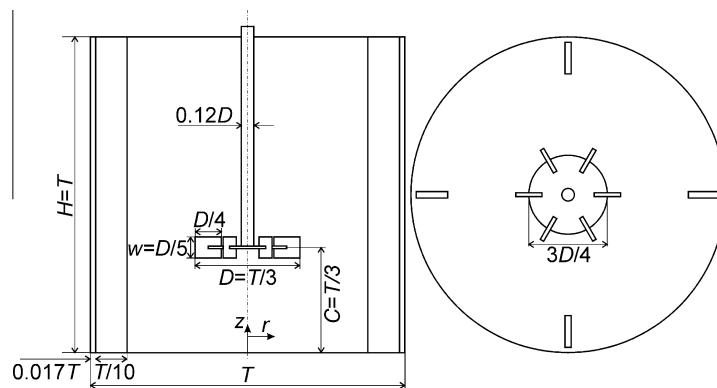
Fig. 4. Stirred tank geometry and (r, z) coordinate system. Left: side view, right: top view.

interests are in how the flow develops towards a (quasi) steady state, what flow structures can be observed in (quasi) steady state, and what the influence of the Deborah number is on all this.

5.1. Results

Fig. 5 shows the development of the tank-average network integrity parameter $\langle \lambda \rangle$ after starting from a zero flow, and zero λ field. Clearly, the higher Db the slower the network develops. In addition, the path along which the three cases approach quasi steady state is very different. At Db = 1 the network builds up quicker than the flow that starts around the impeller can penetrate the bulk of the tank. This results in an initial overshoot of $\langle \lambda \rangle$ with λ quickly increasing in the still quiescent parts of the tank. In a later stage the flow erodes the networked zones in the tank and $\langle \lambda \rangle$ decreases again after which a quasi steady state is reached. For Db = 10 the development towards steady-state has a relatively fast stage (with a time scale associated to it of the order of k_2^{-1}) and a slow stage taking of the order of 150 impeller revolutions. At the highest Db (Db = 100) the system very gradually goes towards steady state.

The Db = 1 case gives rise to a very inhomogeneous distribution of the apparent viscosity in the tank, with low levels close to the impeller and in the stream emerging from the impeller where the network is destroyed continuously due to liquid deformation, and high levels in the dead zones in (for instance) the upper corners (see Fig. 6, upper center panel). This
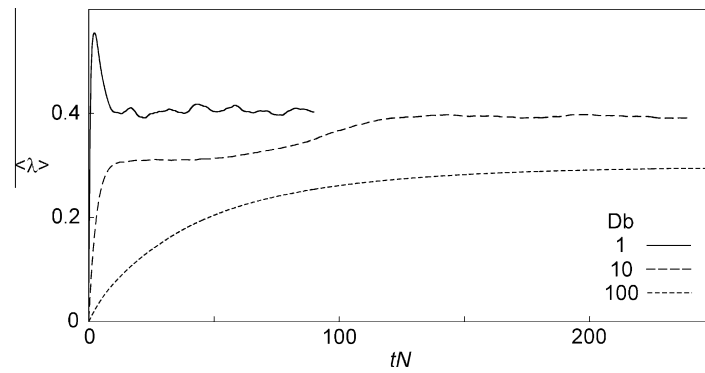

Fig. 5. Time series of the tank-averaged λ for three values of Db when starting up from a zero flow, and zero λ field.
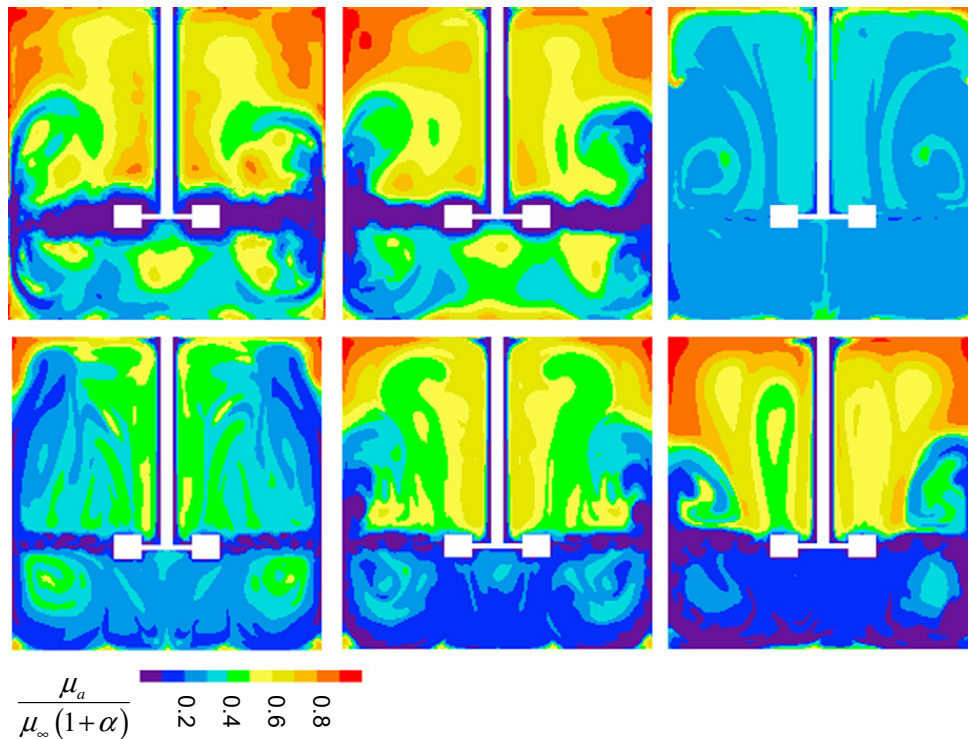

Fig. 6. Snapshots of the apparent viscosity in a vertical cross section through the tank. Top row from left to right: Db = 0 at tN = 60, Db = 1 at tN = 60, Db = 100 at tN = 250. Bottom row: Db = 10 and (from left to right) tN = 50, 100, 210.

distribution creates active and relatively inactive regions in the tank. For comparison Fig. 6 (upper left panel) also displays a distribution of the apparent viscosity if Db = 0, which we get if instead of a thixotropic liquid we have a time independent liquid with the steady-state apparent viscosity of Eq. (3). The apparent viscosity distribution with Db = 1 is very similar to the one with Db = 0 indicating that for Db = 1 (and the rest of the current conditions: flow geometry, other dimensionless numbers) the time dependence of the liquid is not strongly felt.

If Db = 100, the liquid's time scales are much longer than almost all relevant flow time scales. In other words, the mixing is very fast compared to the build-up and breakdown of the network which leads to a fairly uniform (well-mixed) distribution of the apparent viscosity, see Fig. 6 (upper right panel). This situation is comparable to a very slow chemical reaction taking place in a vigorously mixed tank. Under such conditions the tank can be considered ideally mixed with approximately uniformly distributed concentrations. At the specific settings of this simulation, the level of the apparent viscosity ultimately gets of the order of $20\mu_\infty$ throughout the tank which corresponds to a Reynolds number of $\mathrm{Re}_a = \frac{\rho N D^2}{\mu_a} \approx 300$, indicating transitional flow.

The most intriguing case of Fig. 5 is the one with Db = 10. Some 20 revolutions after startup the system tends to steady state. However, beyond 50 revolutions $\langle \lambda \rangle$ starts slowly but systematically increasing again until it levels off after 150 revolutions after start-up. What happens in the slow part of the flow's development (between 50 and 150 revolutions) is a slow build-up of the network in the upper part of the tank which gradually pushes the impeller stream down until the liquids only recirculates underneath the impeller, see Fig. 6 (lower three panels).

6. Suspensions involving thixotropic liquids

Dense solid–liquid suspensions involving non-Newtonian carrier fluids are of practical relevance in applications such as oil sands mining, drilling of oil and gas wells, and food and pharmaceutical processing. Fundamental insights in the interactions of solid and liquid at the level of the solid particles could be relevant for a better understanding of the processes underlying these applications, and thus could help in process design and optimization. Also, process modeling (partly) based on computational fluid dynamics (CFD) at the macro-scale has become a viable and widely used approach. Multiphase CFD, however, requires closure relations for meso-scale phenomena such as the hydrodynamic interaction between the phases involved [22]. A lot of research effort has been invested in developing and assessing closures for multiphase systems with a Newtonian carrier phase, such as drag force relations for random particle assemblies [23,24], and models for turbulent and granular fluctuations. In situations where the carrier phase behaves as a non-Newtonian liquid, the meso-scale fluid mechanics (hydrodynamic interactions, dispersed phase behavior) potentially becomes more complicated. This may have significant implications for the applicability of closures (based on Newtonian fluid concepts) for the meso-scale phenomena of suspensions with non-Newtonian liquids.

With the above in mind we have carried out computational research that aims at assessing non-Newtonian effects in dense solid–liquid suspensions, with a focus on the drag force and the way it depends on liquid properties and the solids volume fraction. The study is limited to suspensions consisting of monodisperse spheres with diameter d in a purely viscous thixotropic carrier liquid described by Eqs. (1) and (2). The sphere assemblies with solids volume fraction ϕ are random and homogeneous; there are no large-scale (solids volume fraction) gradients. The liquid is forced through the spheres with a superficial velocity u_s such that the flow is slow, i.e. dominated by viscous forces rather than inertia. The computations measure the drag force on the spheres. The average drag force on a sphere F_D is normalized with the Stokes drag on a sphere in a Newtonian liquid with viscosity μ_∞: $F_D^* \equiv \frac{F_D}{3\pi\mu_\infty d u_s}$.

The flow of thixotropic liquids through monosized sphere assemblies can be pinned down with a set of five dimensionless numbers. In this paper these have been chosen as $\mathrm{Re}_\infty = \frac{\rho u_s d}{\mu_\infty}$, $\mathrm{Db} = \frac{u_s}{dk_2}$, $\mathrm{S} = \frac{\dot{\gamma}_c d}{u_s}$, α, and ϕ. This five-dimensional parameter space has been limited by only considering a single, low value of $\mathrm{Re}_\infty = 0.06$. We also fix the viscosity ratio to $\alpha + 1 = 16$. Since $\alpha > 0$ the low value of the Reynolds number implies creeping flow conditions at all times.

The resolution of the simulations is such that the sphere diameter d is equal to 24 grid spacings. The diameter d is the so-called hydrodynamic diameter of the spheres. A calibration procedure [25] is used to relate the hydrodynamic diameter to the diameter in the lattice. This calibration slightly depends on the viscosity, it has been carried out for $\mu = \mu_\infty\left(1 + \frac{1}{2}\alpha\right)$.

6.1. Results for shear-thinning time independent liquids

Time-independent liquids have $k_2 \to \infty$ so that Db = 0. The two degrees of freedom left are the solids volume fraction ϕ and $\mathrm{S} = \frac{\dot{\gamma}_c d}{u_s}$.

Fig. 7 shows contour plots of the distribution of the apparent viscosity in a cross section through the suspension after steady state has been reached. The cross sections span the *xz*-plane of the cubic periodic domain with the *x*-direction the streamwise direction. The white circular disks are cross sections through the spherical particles. The higher S, the higher the apparent viscosity in the suspension gets. This is not surprising. At higher S (and thus higher $\dot{\gamma}_c$) the transition from zero-shear viscosity to infinite-shear viscosity takes place at higher shear rates (see Fig. 1). Also the range of viscosities encountered in the suspension is a function of S: if the characteristic shear rate $\dot{\gamma}_c$ of the liquid is of the same order as the shear rates encountered in the interstitial liquid, a relatively broad range of viscosities is anticipated.
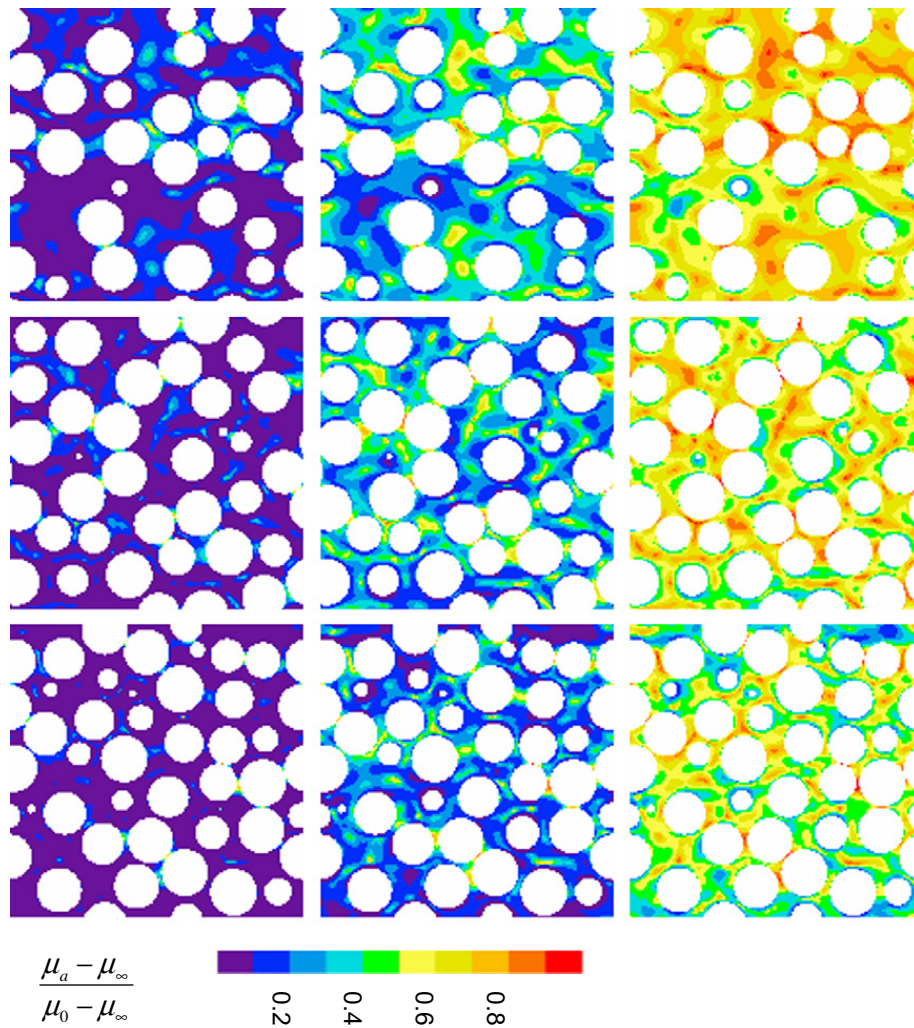
Fig. 7. xz-Cross sections through the flow domains, with the horizontal (x) direction the direction of the mean flow. Shear-thinning, time-independent liquids. Colors indicate the apparent viscosity. From top to bottom $\phi = 0.373$, 0.459, and 0.530. From let to right S = 1, 4, and 16 respectively.

The above observations are presented in a more quantitative sense in Fig. 8. The figure shows (for two solids volume fractions) the doubly normalized drag force $F_D^{**} \equiv \frac{F_D^*}{F_D^*|_{S=0}}$, the average apparent viscosity in the suspension, and (as a measure of the spread in viscosities in the liquid domain) the root-mean-square (rms) values of the deviations from the mean apparent viscosity. Interestingly rms(μ_a) goes through a maximum with the location of the maximum dependent on the solids volume fraction: the higher ϕ the further the maximum shifts to higher S. At higher ϕ the space between the spheres gets narrower and (since the superficial velocity has a fixed value) the deformation rates in the liquid increase. As a result, the distribution of viscosities gets wider for higher S.

Eventually, the drag force is the result of an interplay between the liquid flow through the suspension and the resulting spatial viscosity distribution. The notion of the interaction between $\dot{\gamma}_c$ and deformation rates in the suspensions proofs helpful in scaling the doubly normalized drag force F_D^{**}. Critical regions in the suspension are the waists between nearby spheres. As a measure for the size of these waists we take $\delta \equiv d\left[\left(\frac{\phi_{rcp}}{\phi}\right)^{1/3} - 1\right]$ with $\phi_{rcp} = 0.62$ the solids volume fraction at random close packing. In Fig. 9 we plot F_D^{**} as a function of $\frac{\delta \dot{\gamma}_c}{u_s}$ for all cases with time-independent rheology (Db = 0) considered. The drag force behaves fairly consistently over the wide range of solids volume fractions considered.

6.2. Results for thixotropic liquids

Examples of steady-state viscosity distributions with thixotropic liquids are given in Fig. 10. The most visible effect of thixotropy is a smearing-out of the viscosity fluctuations. This effect sets in beyond Db = 0.2 (the viscosity fields at Db = 0 and Db = 0.2 are almost the same). The smearing out is due to the time it takes to build up or break down the network. In an infinitely fast (Db = 0) liquid, locations where the network is formed or broken down coincide with places of
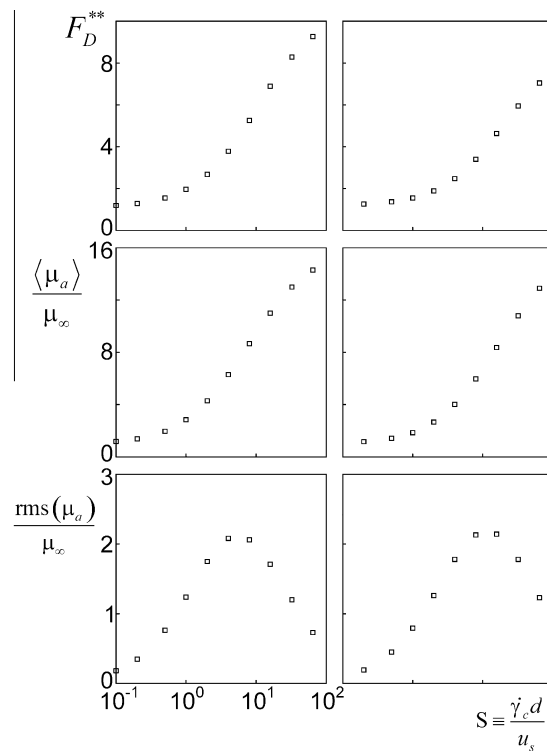
Fig. 8. Doubly normalized drag force F_D^{**} (top); average apparent viscosity (middle); and root-mean-square values of the apparent viscosity as a function of S for two solids volume fractions: left: $\phi = 0.373$, $\phi = 0.530$. Shear-thinning, time-independent liquids.
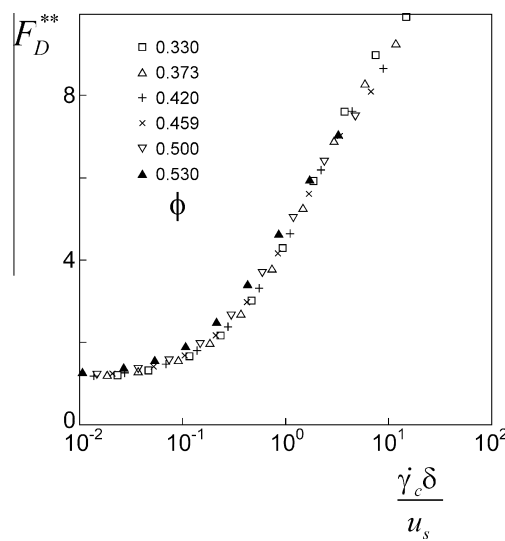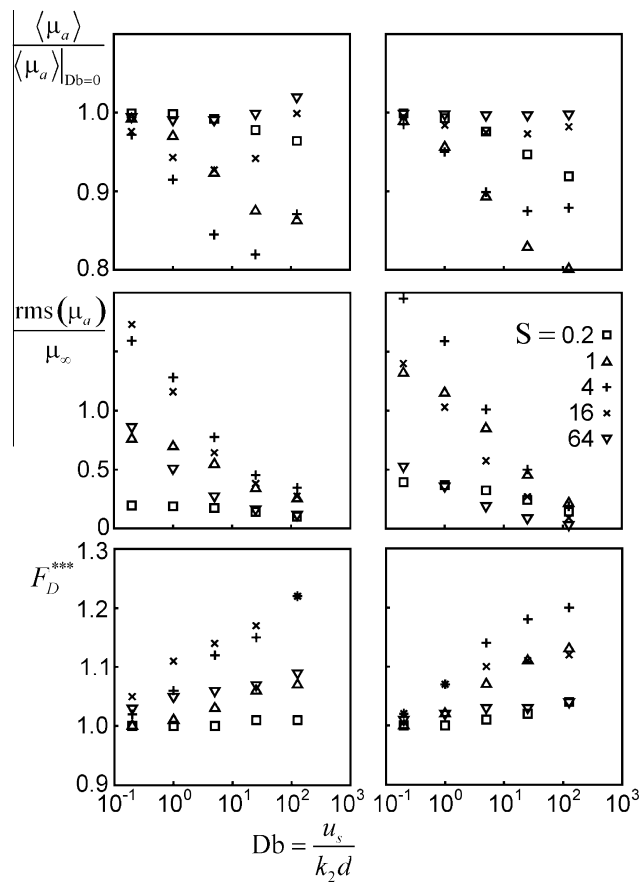

Fig. 9. Doubly normalized drag force as a function of $\frac{\delta\dot{\gamma}_c}{u_s}$ with δ defined in the text. The different symbols relate to different solids volume fraction as indicated. Shear-thinning, time-independent liquids.

respectively low (e.g. bigger voids in the suspension) and high (shear layers at solid surfaces) deformation rates. If the liquid needs time to respond to deformation conditions (Db > 0) the break-down and build-up processes are less localized with a smoother apparent viscosity field as the result.

In Fig. 11 sample results of our thixotropic simulations are displayed, with Db as the independent variable. The triply normalized drag force is defined as $F_D^{***} \equiv \frac{F_D^{**}}{F_D^{**}\big|_{Db=0}}$. In the way as displayed in Fig. 11, the behavior is quite similar for different solids volume fractions, so that we only show the extremes of ϕ as studied here. The effect of a smoother apparent viscosity field due to thixotropy is an increase in the drag force; in all cases considered $F_D^{***} > 1$. The effect of thixotropy on the drag force is not very big; the maximum increase is approximately 20%, occurring for high Db in situations where the corresponding Db = 0 system had a large rms(μ_a).
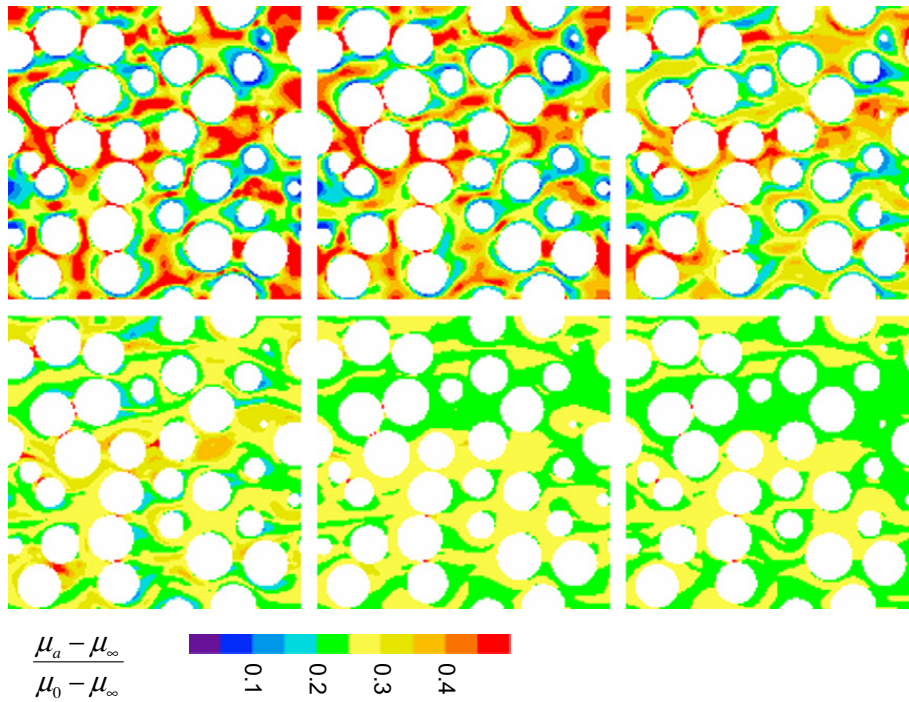
Fig. 10. *xz*-Cross sections through one flow domain, with the horizontal (*x*) direction the direction of the mean flow. $\phi = 0.420$, S = 4. Thixotropic simulations with (from left to right and top to bottom) Db = 0, 0.2, 1.0, 5.0, 25.0, 125.0. Colors indicate the apparent viscosity.

Fig. 11. Sample simulation results with thixotropic liquids. From bottom to top: triply normalized drag force, rms of viscosity, and average viscosity as a function of Db. Left: $\phi = 0.530$; right: $\phi = 0.330$. The different symbols denote different values of S as indicated.

7. Summary

In this paper simulations at the equipment (macro) scale and at the particle (meso) scale of the flow of thixotropic liquids have been described. Geometrical complexity (mixing tanks, interstitial liquid in suspensions) was essential in these applications. Purely viscous thixotropic behavior can be simulated with a Navier–Stokes solver that is able to handle variable viscosity, combined with a (non-diffusive) scalar transport solver for keeping track of local network integrity. The network integrity is fed back to the Navier–Stokes solver by means of a relation between network integrity and apparent viscosity. As the Navier–Stokes solver a lattice-Boltzmann scheme has been employed and for solving the scalar transport equation a finite volume solver with TVD discretization; the latter for minimizing numerical diffusion. The feasibility and accuracy of the approach was assessed with a plane Poiseuille flow benchmark.

Applying this approach to laminar and transitional stirred tank flow showed the essential role of the liquid's time scale on the overall flow behavior in the tank. Liquids with the same steady state rheology, but different time response (i.e. flow systems with different Deborah number) evolve differently towards markedly different steady states. At $Db = \frac{N}{k_2} = 1$ the liquid behaves almost the same as its infinitely fast, shear thinning equivalent. At $Db = 100$ the liquid is so slow compared to mixing that the level of network development is typically uniform in the tank leading (in the case investigated here) to laminar flow. At the in-between Deborah number of 10 the flow develops in a peculiar manner, being the result of a subtle interplay between flow and liquid time scales. In this latter case the liquid is mobilized in a limited portion of the tank volume only.

Subsequently we studied drag forces in random, monosized sphere assemblies immersed in shear thinning and thixotropic liquids. As a result of the tortuous flow through the sphere assembly and its associated broad spectrum of deformation rates, shear thinning effects on drag are significant with a strong influence of the solids volume fraction (the higher, the more tortuous the flow). The effect of the solids volume fraction could be quite well captured by scaling the liquids characteristic shear rate with the superficial velocity over the average waist of two neighbouring spheres. The effect of thixotropy is a smoothing effect on the apparent viscosity in the suspension, which in general leads to increased (by some 20%) drag.

An essential feature when studying thixotropic – and more generally non-Newtonian – flow is the rapid growth of the parameter space with increasing complexity of the liquid model. As an example: in Newtonian stirred tank flow – once the flow geometry has been defined – the only dimensionless number that matters is the Reynolds number (assuming there is no free liquid surface). In this paper (with a relatively simple liquid model) we needed four dimensionless groups to pin down the flow. This makes our results less general (i.e. more specific to the model used). However, the tools developed here can be used to study specific (industrial) liquids. Furthermore, the simulations do show interesting features related to liquid mobility (in mixing tanks) and drag force behavior (in solid–liquid suspensions).

References

[1] J. Masliyah, Z.J. Zhou, Z. Xu, J. Czarnecki, H. Hamza, Understanding water-based bitumen extraction from Athabasca oil sands, Can. J. Chem. Eng. 82 (2004) 628–654.
[2] J. Derksen, H.E.A. Van den Akker, Large-eddy simulations on the flow driven by a Rushton turbine, AIChE J. 45 (1999) 209–221.
[3] H. Hartmann, J.J. Derksen, C. Montavon, J. Pearson, I.S. Hamill, H.E.A. Van den Akker, Assessment of large eddy and RANS stirred tank simulations by means of LDA, Chem. Eng. Sci. 59 (2004) 2419–2432.
[4] S. Succi, The Lattice Boltzmann Equation for Fluid Dynamics and Beyond, Clarondon Press, Oxford, 2001.
[5] B.T. Storey, E.W. Merrill, The rheology of aqueous solution of amylose and amylopectine with reference to molecular configuration and intermolecular association, J. Polym. Sci. 33 (1958) 361–375.
[6] F. Moore, The rheology of ceramic slips and bodies, Trans. Brit. Ceramic Soc. 58 (1959) 470–494.
[7] A. Mujumdar, A.N. Beris, A.B. Metzner, Transient phenomena in thixotropic systems, J. Non-Newton. Fluid Mech. 102 (2002) 157–178.
[8] U. Frisch, B. Hasslacher, Y. Pomeau, Lattice-gas automata for the Navier–Stokes equation, Phys. Rev. Lett. 56 (1986) 1505–1508.
[9] S. Chen, G.D. Doolen, Lattice Boltzmann method for fluid flows, Annu. Rev. Fluid Mech. 30 (1998) 329–364.
[10] M.C. Sukop, D.T. Thorne Jr., Lattice Boltzmann Modeling: An Introduction for Geoscientists and Engineers, Springer, Berlin, 2006.
[11] M. Yoshino, Y. Hotta, T. Hirozane, M. Endo, A numerical method for incompressible non-Newtonian fluid flows based on the lattice Boltzmann method, J. Non-Newton. Fluid Mech. 147 (2007) 69–78.
[12] A. Vikhansky, Lattice-Boltzmann method for yield-stress liquids, J. Non-Newton. Fluid Mech. 155 (2008) 95–100.
[13] J.A. Somers, Direct simulation of fluid flow with cellular automata and the lattice-Boltzmann equation, Appl. Sci. Res. 51 (1993) 127–133.
[14] D. Goldstein, R. Handler, L. Sirovich, Modeling a no-slip flow boundary with an external force field, J. Comput. Phys. 105 (1993) 354–366.
[15] J.J. Derksen, Simulation of vortex core precession in a reverse-flow cyclone, AIChE J. 46 (2000) 1317–1331.
[16] J.J. Derksen, Simulations of confined turbulent vortex flow, Comput. Fluids 34 (2005) 301–318.
[17] J.G.M. Eggels, J.A. Somers, Numerical simulation of free convective flow using the lattice-Boltzmann scheme, Int. J. Heat Fluid Flow 16 (1995) 357–364.
[18] H. Hartmann, J.J. Derksen, H.E.A. Van den Akker, Numerical simulation of a dissolution process in a stirred tank reactor, Chem. Eng. Sci. 61 (2006) 3025–3032.
[19] J.J. Derksen, Scalar mixing by granular particles, AIChE J. 54 (2008) 1741–1747.
[20] P.K. Sweby, High resolution schemes using flux limiters for hyperbolic conservation laws, SIAM J. Numer. Anal. 21 (1984) 995–1011.
[21] K. Dullaert, J. Mewis, Thixotropy: build-up and breakdown curves during flow, J. Rheol. 49 (2005) 1213–1230.
[22] J. Li, J.A.M. Kuipers, Gas–particle interactions in dense gas-fluidized beds, Chem. Eng. Sci. 58 (2003) 711–718.
[23] D. Kandhai, J.J. Derksen, H.E.A. Van den Akker, Interphase drag coefficients in gas–solid flows, AIChE J. 49 (2003) 1060–1065.
[24] M.A. Van der Hoef, R. Beetstra, J.A.M. Kuipers, Lattice-Boltzmann simulations of low-Reynolds-number flow past mono- and bidisperse arrays of spheres: results for the permeability and drag force, J. Fluid Mech. 528 (2005) 233–254.
[25] A.J.C. Ladd, Numerical simulations of particle suspensions via a discretized Boltzmann equation – Part 2. Numerical results, J. Fluid Mech. 271 (1994) 311–339.